Video Article

Uncoupling Coriolis Force and Rotating Buoyancy Effects on Full-Field Heat Transfer Properties of a Rotating Channel

Shyy Woei Chang[1], Wei-Ling Cai[1], Hong-Da Shen[1], Kuo-Ching Yu[1]

[1]Department of System and Naval Mechatronic Engineering, National Cheng Kung University

Correspondence to: Shyy Woei Chang at swchang@mail.ncku.edu.tw

URL: https://www.jove.com/video/57630
DOI: doi:10.3791/57630

Keywords: Engineering, Issue 140, Rotating Channel Flow, Heat Convection, Gas Turbine Rotor Blade Cooling, Orthogonal Mode Rotation, Coriolis Effect, Rotating Buoyancy Effect

Date Published: 10/5/2018

Citation: Chang, S.W., Cai, W.L., Shen, H.D., Yu, K.C. Uncoupling Coriolis Force and Rotating Buoyancy Effects on Full-Field Heat Transfer Properties of a Rotating Channel. *J. Vis. Exp.* (140), e57630, doi:10.3791/57630 (2018).

Abstract

An experimental method for exploring the heat transfer characteristics of an axially rotating channel is proposed. The governing flow parameters that characterize the transport phenomena in a rotating channel are identified via the parametric analysis of the momentum and energy equations referring to a rotating frame of reference. Based on these dimensionless flow equations, an experimental strategy that links the design of the test module, the experimental program and the data analysis is formulated with the attempt to reveal the isolated Coriolis-force and buoyancy effects on heat transfer performances. The effects of Coriolis force and rotating buoyancy are illustrated using the selective results measured from rotating channels with various geometries. While the Coriolis-force and rotating-buoyancy impacts share several common features among the various rotating channels, the unique heat transfer signatures are found in association with the flow direction, the channel shape and the arrangement of heat transfer enhancement devices. Regardless of the flow configurations of the rotating channels, the presented experimental method enables the development of physically consistent heat transfer correlations that permit the evaluation of isolated and interdependent Coriolis-force and rotating-buoyancy effects on the heat transfer properties of rotating channels.

Video Link

The video component of this article can be found at https://www.jove.com/video/57630/

Introduction

While thermodynamic laws dictate the improved specific power and thermal efficiency of a gas turbine engine by elevating the turbine entry temperature, several hot engine components, such as turbine blades, are prone to thermal damage. Internal cooling of a gas turbine rotor blade permits a turbine entry temperature in excess of the temperature limits of the creep resistance of the blade material. However, the configurations of the internal cooling channels must comply with the blade profile. In particular, the coolant rotates within the rotor blade. With such harsh thermal conditions for a running gas turbine rotor blade, an effective blade cooling scheme is crucial to ensure the structure's integrity. Thus, the local heat transfer properties for a rotating channel are important for the efficient usage of the limited coolant flow available. The acquisition of useful heat transfer data that are applicable to the design of the internal coolant passages at realistic engine conditions is of primary importance when an experimental method is developed for measuring the heat transfer properties of a simulated cooling passage inside a gas turbine rotor blade.

Rotation at a speed above 10,000 rpm considerably alters the cooling performance of a rotating channel inside a gas turbine rotor blade. The identification of engine conditions for such a rotating channel is permissible using the similarity law. With rotation, the dimensionless groups that control the transport phenomena inside a radially rotating channel can be revealed by deriving the flow equations relative to a rotating frame of reference. Morris[1] has derived the momentum conservation equation of flow relative to a rotating frame of reference as:

$$\frac{\mathrm{D}\bar{v}}{\mathrm{D}t} + 2(\omega \times \bar{v}) - \beta\left(T - T_{ref}\right)(\omega \times \omega \times \bar{r}) = -\frac{1}{\rho_{ref}}\nabla P^{*} + \nu\nabla^{2}\bar{v} \quad (1)$$

In equation (1), the local fluid velocity, $\bar{v}$, with the position vector, $\bar{r}$, relative to a frame of reference rotating at the angular velocity, ω, is affected by the Coriolis acceleration in terms of $2(\omega\times\bar{v})$, the decoupled centripetal buoyancy force, $\beta(T\text{-}T_{ref})(\omega\times\omega\times\bar{r})$, the driven piezo-metric pressure gradient, ∇P^{*}, and the fluid dynamic viscosity, ν. The referenced fluid density, ρ_{ref}, is referred to a pre-defined fluid reference temperature T_{ref}, which is typical of the local fluid bulk temperature for experiments. If the irreversible conversion of mechanical energy into thermal energy is negligible, the energy conservation equation is reduced to:

$$\rho C_{p}\frac{\mathrm{D}T}{\mathrm{D}t} = k_{f}\nabla^{2}T \quad (2)$$

The first term of equation (2) is obtained by treating the specific enthalpy to be directly related to the local fluid temperature, T, via the constant specific heat, C_p. As the perturbation of fluid density caused by the variation of fluid temperature in a heated rotating channel provides considerable influence on the motion of fluids when it links with the centripetal acceleration in equation (1), the fluid velocity and temperature fields in an axially rotating channel are coupled. Also, both Coriolis and centripetal accelerations vary simultaneously as the rotating speed is adjusted. Thus, the effects of Coriolis force and rotating buoyancy on the fields of fluid velocity and temperature are naturally coupled.

Equations (1) and (2) in the dimensionless forms disclose the flow parameters that govern the heat convection in a rotating channel. With a basically uniform heat flux imposed on a rotating channel, the local fluid bulk temperature, T_b, increases linearly in the streamwise direction, s, from the reference inlet level, T_{ref}. The local fluid bulk temperature is determined as $T_{ref} + \tau s$, where τ is the gradient of the fluid bulk temperature in the direction of flow. Substitutions of the following dimensionless parameters of:

$$\vec{V} = \bar{v}/V_{mean} \quad (3)$$

$$\Omega = \omega/N \quad (4)$$

$$\vec{R} = \bar{r}/d \quad (5)$$

$$\lambda = P^*/(\rho_{ref} V_{mean}^2) \quad (6)$$

$$\eta = (T - T_{ref})/(\tau d) \quad (7)$$

into equations (1) and (2), where V_{mean}, N and d respectively stand for the mean flow through velocity, rotating velocity and channel hydraulic diameter, the dimensionless flow momentum and energy equations are derived as equations (8) and (9) respectively.

$$\frac{D\vec{V}}{Dt} + Ro\left(2\Omega \times \vec{V}\right) - Ro^2 \beta \tau d\eta\left(\Omega \times \Omega \times \vec{R}\right) = -\nabla\lambda + \frac{1}{Re}\nabla^2\vec{V} \quad (8)$$

$$\frac{D\eta}{Dt} = \frac{1}{RePr}\nabla^2\eta \quad (9)$$

Evidently, η in equation (9) is a function of Re, Ro, and $Bu = Ro^2\beta\tau dR$, which are respectively referred to as Reynolds, rotation and buoyancy numbers. The Rossby number that quantifies the ratio between inertial and Coriolis forces is equivalent to the inverse rotation number in equation (8).

When T_b is calculated as $T_{ref} + \tau s$ in a rotating channel subject to a uniform heat flux, the τ value can be alternatively evaluated as $Q_f/(mC_pL)$ in which Q_f, m and L are the convective heating power, coolant mass flow rate and channel length, respectively. Thus, the dimensionless local fluid bulk temperature, η_b, is equal to s/d and the dimensionless temperature at channel wall, η_w, yields $[(T_w\text{-}T_b)/Q_f][mC_p][L/d]+s/d$. With the convective heat transfer rate defined as $Q_f/(T_w\text{-}T_b)$, the dimensionless wall-to-fluid temperature difference, $\eta_w\text{-}\eta_b$, is convertible into the local Nusselt number via equation (10) in which ζ is the dimensionless shape function of heating area and channel sectional area.

$$Nu(s) = \zeta \frac{RePr}{\eta_w(s) - \eta_b(s)} \quad (10)$$

With a set of predefined geometries and the hydrodynamic and thermal boundary conditions, the dimensionless groups controlling the local Nusselt number of a rotating channel are identified as:

$$Re = V_{mean} d/v \quad (11)$$

$$Ro = Nd/V_{mean} \quad (12)$$

$$Bu = Ro^2 \beta \tau dR \quad (13)$$

With experimental tests, the adjustment of rotating speed, N, for varying Ro to generate the heat transfer data at different strengths of Coriolis forces inevitably changes the centripetal acceleration, and thus, the relative strength of rotating buoyancy. Moreover, a set of heat transfer data collected from a rotating channel is always subject to a finite degree of rotating buoyancy effect. To disclose the individual effects of Coriolis-force and buoyancy on the heat transfer performance of a rotating channel requires the uncoupling of the Ro and Bu effects on Nu properties through the post data processing procedure that is inclusive in the present experimental method.

The engine and laboratory flow conditions for a rotating channel inside a gas turbine rotor blade can be specified by the ranges of Re, Ro and Bu. The typical engine conditions for the coolant flow through a gas turbine rotor blade, as well as the construction and commissioning of the rotating test facility that allowed experiments to be performed near the actual engine conditions was reported by Morris[2]. Based on the realistic engine conditions summarized by Morris[2], **Figure 1** constructs the realistic operating conditions in terms of Re, Ro and Bu ranges for a rotating coolant channel in a gas turbine rotor blade. In **Figure 1**, the indication of an engine's worst condition is referred to as the engine running condition at the highest rotor speed and the highest density ratio. In **Figure 1**, the lower limit and worst engine operating conditions respectively emerge at the lowest and highest engine speeds. It is extremely difficult to measure the full-field Nu distribution of a rotating channel running at a real engine speed between 5000 and 20,000 rpm. However, based on the similarity law, laboratory-scale tests have been conducted at reduced rotating speeds but with several attempts to provide a full coverage of the real-engine Re, Ro and Bu ranges. As an innovative experimental

method, the NASA HOST program[3,4,5,6] adopted the high-pressure tests for increasing the fluid densities at the predefined *Re* in order to extend the *Ro* range by reducing the mean fluid velocity. In this regard, the specific relationships between *Re*, *Ro* and *Bu* for an ideal gas with a gas constant, R_c, and viscosity, μ, are related as:

$$Ro = Re^{-1}(Pd^2N)/(R_cT_b\mu) \quad (14)$$

$$Bu = Ro^2R(T_w - T_b)/T_b \quad (15)$$

To bring the laboratory conditions into the nominal correspondence with engine conditions seen in **Figure 1**, the rotating speed, *N*, coolant pressure, *P*, channel hydraulic diameter, *d*, rotating radius, *R*, and wall-to-fluid temperature difference, T_w-T_b, need to be controlled for matching the realistic *Re*, *Ro* and *Bu* ranges. Clearly, one of the most effective approaches to extend the *Ro* range is to increase channel hydraulic diameter, as *Ro* is proportional to d^2. As the laboratory heat transfer test at realistic *N* is extremely difficult, the coolant pressure, *P*, is technically easier to be raised for extending *Ro* range; even if *Ro* is only proportional to *P*. Based on this theoretical background, the design philosophy of the present experimental method is to increase *Ro* by pressurizing the rotating test channel using the maximum channel hydraulic diameter allowed to fit into the rotating rig. Having increased the *Ro* range, the range of *Bu* is accordingly extended as *Bu* is proportional to Ro^2. In **Figure 1**, the laboratory test conditions adopted to generate the heat transfer data of rotating channels are also included[3,4,5,6,7,8,9,10,11,12,13,14,15,16,17,18,19,20,21,22,23,24,25,26,27,28,29]. As indicated in **Figure 1**, the coverage of realistic engine conditions by the available heat transfer data is still limited, especially for the required *Bu* range. The open and the colored solid symbols depicted in **Figure 1** are the pointed and full-field heat transfer experiments, respectively. As collected in **Figure 1**, most of the heat transfer data with cooling applications to gas turbine rotor blades[1,2,3,4,5,6,7,8,9,10,11,12,13,14,15,16,17,18,20,21,22,23,24,25,26] are point measurements using the thermocouple method. The wall conduction effects on measuring the wall conductive heat flux and the temperatures at fluid-wall interfaces undermine the quality of heat transfer data converted from the thermocouple measurements. Also, the heat transfer measurements[1,2,3,4,5,6,7,8,9,10,11,12,13,14,15,16,17,18,20,21,22,23,24,25,26] using the thermocouple method cannot detect the two-dimensional heat transfer variations over a rotating surface. With the present experimental method[29,30,31,32], the detection of full-field Nusselt number distributions over the rotating channel wall is permissible. The minimization of wall conduction effect using 0.1 mm thick stainless-steel foils with Biot numbers >>1 to generate the heating power by the present experimental method permits the one-dimensional heat conduction from the heating foil to the coolant flow. In particular, the acquisition of full-field heat transfer data involving both *Ro* and *Bu* effects is not permissible using the transient liquid crystal technique and the thermocouple method. With the current steady-state liquid crystal thermography method[19], the detectable temperature range of 35-55 °C disables the generation of heat transfer data with realistic density ratios.

Using the flow parameters governing the heat convection in a rotating channel to demonstrate that the full coverage of realistic engine conditions seen in **Figure 1** has not yet been achieved, so the need for acquiring the full-field heat transfer data at realistic engine conditions has been continuously urged. The present experimental method enables the generation of full-field heat transfer with both Coriolis-force and rotating-buoyancy effects detected. The protocols are aimed at assisting the investigators to devise an experimental strategy relevant to the realistic full-field heat transfer measurement of a rotating channel. Along with the method of parametric analysis that is unique to the present experimental method, the generation of heat transfer correlation for assessing the isolated and interdependent *Ro* and *Bu* effects on *Nu* is permitted.

The article illustrates an experimental method aimed at generating the two-dimensional heat transfer data of a rotating channel with flow conditions similar to the realistic gas turbine engine conditions but operating at much lower rotating speeds in the laboratories. The method developed to select the rotating speed, the hydraulic diameter of test channel and the range of wall-to-fluid temperature differences for acquiring the heat transfer data at realistic engine conditions is illustrated in the introduction. The calibration tests for the infrared thermography system, the heat loss calibration tests and the operation of the rotating heat transfer test rig are shown. The factors causing the significant uncertainties for heat transfer measurements and the procedures for decoupling the Coriolis-force and buoyancy effects on the heat transfer properties of a rotating channel are described in the article with the selective results to demonstrate the present experimental method.

Protocol

NOTE: The details of rotating test facilities, data acquisition, data processing and the heat transfer test module emulating an internal cooling channel of a gas turbine rotor blade are in our previous works[29,30,31,32].

1. Preparation of Heat Transfer Tests

1. Formulate the experimental conditions in terms of *Re*, *Ro* and *Bu* from the targeted operation conditions of a gas turbine rotor blade.
2. Determine the *N*, *P*, *d*, *R*, and T_w - T_b needed for acquiring the tested *Re*, *Ro* and *Bu* using equations (14) and (15).
3. Re-define the targeting *Re*, *Ro* and *Bu* if *N*, *P*, *d*, *R*, and T_w - T_b exceeds the limit of the experimental facilities.
4. Design and construct the scaled heat transfer test module emulating a practical internal coolant channel in a gas turbine rotor blade[2].

2. Determination of Thermal Emissivity Coefficient for Infrared Thermography System

1. Install the calibrated thermocouple on the back side of the scanned stainless-steel heating foil.
2. Spray a thin layer of black paint on the stainless-steel heating foil scanned by the infrared camera.
3. Create symmetrical flow fields on two sides of the stainless-steel heating foil by placing a vertical thin stainless-steel foil in a space with the free convective flows over the two sides of the vertical heating foil.
4. Feed electrical heating power through the heating foil and measure temperatures simultaneously by thermocouple and infrared thermography system from the computer display at steady state.
5. Repeat step 2.4 at least four times using elevated heater powers. Ensure that the wall temperatures corresponding to the heater powers used by steps 2.3 and 2.4 cover the T_w range determined by step 1.2.

6. Calculate the T_w values scanned by the infrared thermography system using a number of selective thermal emissivity coefficients for the program that converts the infrared signals into temperature data.
7. Compare the T_w data measured by the calibrated thermocouple and the infrared thermography system at the location corresponding to the thermocouple spot with the standard deviations evaluated.
8. Select the thermal emissivity coefficient with the minimum standard deviation determined by step 2.7.
9. Determine the maximum precision error for the infrared thermography system using the thermal emissivity coefficient determined by step 2.8.

3. Dynamic Balance of Rotating Rig

1. Install the heat transfer test module, the infrared camera, the enveloping frame and all accessories on the rotating rig.
2. Adjust the counterbalancing weight gradually until the running condition of the rotating rig satisfies the vibrational limitation for the infrared thermographic measurements to exhibit the stable thermal image on the computer display.

4. Evaluation of Heat Loss Coefficients

1. Fill the coolant channel of the heat transfer test module with thermal insulation material.
2. Install the filled test module on the rotating test rig by fitting the test module on the rotating platform and connecting the heater power supply and all the instrumental cables.
3. Activate the data acquisition system to scan the temporal T_w variation at a heating power until the steady state condition is satisfied. Ensure that the temporal T_w variations during several successive scans are less than +0.3 K at each steady state condition.
4. Record the heater power, steady-state T_w data and the corresponding ambient temperature, T_∞.
5. Repeat steps 4.3 and 4.4 at least five times using different heating powers at a fixed rotating speed.
6. Repeat steps 4.2 - 4.4 with at least five rotating speeds. Ensure that the test range of the rotating speed covers all the *N* values determined by step 1.2.
7. Repeat steps 4.3 - 4.6 with a reversed rotating direction.
8. Construct the plots of heat loss flux against wall-to-ambient temperature difference at each rotating speed.
9. Correlate the heat loss coefficients as the functions of wall-to-ambient temperature difference, rotating speed and direction of rotation.
10. Incorporate the heat loss correlation into the post data process program for *Nu* accountancy.

5. Baseline Heat Transfer Tests

1. Perform heat transfer tests at the targeting Reynolds numbers at zero rotating speed (*Ro* = *N* = 0) by feeding coolant flows and heater powers to the test module. Ensure the supplied coolant mass flow rate is constantly adjusted in order to control Reynolds number at the flow entry plane at the targeting value.
2. Record all the relevant raw data, including the steady state wall temperatures, fluid temperatures, heater powers, flow pressures and ambient pressures and temperatures, for subsequent data processing.
3. Evaluate the local and area-averaged Nusselt numbers (Nu_0) over the scanned static channel walls.

6. Rotating Heat Transfer Tests

1. Install the on-line monitoring program to monitor the test conditions at the targeting *Re* and *Ro*.
2. Feed the measured coolant mass flow rate, airflow pressure, rotating speed and fluid temperature at channel entrance into the monitoring program to calculate the instant *Re* and *Ro*.
3. Record all the relevant raw data, such as rotating speed, heater power, airflow and ambient pressures, as well as the wall and fluid temperatures for subsequent data processing after the pre-defined steady-state condition is satisfied.
4. Repeat steps 6.2 and 6.3 with at least four ascending or descending heater powers at a set of fixed *Re* and *Ro*. Ensure that the test *Re* and *Ro* fall within ±1% differences from the targeting values by adjusting the rotating speed or the coolant mass flow rate or both.
5. Ensure that the heat transfer tests at each set of fixed *Re* and *Ro* with different heater powers are continuously performed as the development of buoyancy induced flows is associated with the "history" of the flow development.
6. Repeat steps 6.4 and 6.5 with four or five targeting Reynolds numbers (*Re*) at a fixed rotation number (Ro). Ensure the rotating speed is appropriately adjusted at each test *Re* to control both *Re* and *Ro* at the targeting values within ±1% differences.
7. Repeat step 6.6 using four or five targeting rotation numbers (Ro).
8. Repeat steps 6.2 to 6.7 with reversed rotating direction.
9. Evaluate the local and area-averaged Nusselt numbers (*Nu*) over the scanned rotating channel walls using a post data processing program.

7. Parametric Analysis

1. Correlate the area-averaged Nusselt numbers (Nu_0) collected from the static channel into the functions of Reynolds number.
2. Evaluate the full-field local Nu/Nu_0 ratios at each fixed *Re* and *Ro* tested with the area-averaged Nu/Nu_0 ratios calculated.
3. Verify the applicability of isolation *Re* effect by plotting the local and area-averaged Nu/Nu_0 ratios obtained with different *Re* but at identical *Ro*.
4. Disclose the isolated impacts of rotating buoyancy on heat transfer properties of the rotating test channel by plotting the area-averaged Nu/Nu_0 ratios collected at the same *Ro* with different *Re* against *Bu* or density ratio ($\Delta\rho/\rho$). Ensure the preferable selection of *Bu* or $\Delta\rho/\rho$ to construct this type of plot for obtaining the consistent data trend with a simple functional structure for heat transfer correlation.
5. Extrapolate each Nu/Nu_0 data trend collected at a fixed *Ro* but different *Re* into the limiting condition of $Bu \rightarrow 0$ or $\Delta\rho/\rho \rightarrow 0$.
6. Collect all the extrapolated Nu/Nu_0 results with $Bu \rightarrow 0$ or $\Delta\rho/\rho \rightarrow 0$ at all the tested *Ro*.

7. Plot the extrapolated Nu/Nu_0 results with vanished buoyancy interaction against *Ro* to disclose the uncoupled Coriolis force effects on the heat transfer properties.
8. Correlate the test results collected by steps 7.4 and 7.7 into the functions of *Ro* and *Bu*.

Representative Results

Realistic operating conditions for the internal coolant flows inside a rotating gas turbine blade in terms of *Re*, *Ro* and *Bu* are compared with the emulated laboratory conditions in **Figure 1**. The data points fall in the realistic engine conditions using the present experimental method summarized in the protocols[11,14,17,20,21]. Although the full-field heat transfer data are more useful than the pointed heat transfer data measured from the rotating channels, most of the previous heat transfer experiments adopt the thermocouple method (**Figure 1**). The present infrared thermography method detects the full-field heat transfer information from a rotating surface with the buoyancy-induced flows fully developed. With the free or forced convective external flows for a static or rotating test channel, the present protocols include the generation of heat loss correlations for post data processing (**Figure 2**). At the top of **Figure 2**, the construction of the heat transfer test module is also demonstrated. The correlative coefficients for all the fitted lines shown by **Figure 2** fall between 0.95-0.98. In view of the h_{loss} correlation seen in the plot of h_{loss} against *N* in **Figure 2**, the error bars indicate the data range determined at each rotating speed.

Figure 3, **Figure 4**, and **Figure 5** depict the selective heat transfer results measured from the static two-pass S-channel with longitudinal wavy ribs, the rotating two-pass S-channel[31] and the rotating furrowed[32] and pin-fin channel[33]. The estimated maximum uncertainties of the *Nu* measurements for the static S-ribbed channel, the rotating S-channel[31], furrowed channel[32] and pin-fin channel[33] are 7.9%, 8.8%, 9.2%, and 9.7%, respectively. To disclose the *Re* impact on the heat transfer properties of a coolant channel, the base-line full-field heat transfer data detected from the static channel by the present infrared thermography method as typified by **Figure 3** are essential. The diagram shown at the top of **Figure 3** also depicts the channel configuration of the two-pass S-channel with the longitudinal wavy ribs. The channel section is square with the semi-circular sectioned longitudinal wavy ribs on two opposite heated walls of the inlet and outlet legs.

The applicability of isolated *Re* impact from *Ro* and *Bu* effects on local and regionally averaged heat transfer is permitted by presenting the heat transfer data in terms of Nu/Nu_0 (**Figure 4**). Both patterns and levels of Nu/Nu_0 at the same *Ro* with similar *Bu* seem to be weak functions of *Re* (**Figure 4**). The typical results from the protocol for disclosing the isolated Coriolis force effects on heat transfer properties are demonstrated in **Figure 5**. In **Figure 5**, the variations of Nu/Nu_0 at each fixed *Ro* against *Bu* for two different rotating channels with wavy endwalls[32] and diamond shaped pin-fins[33] tend to follow linear-like data trends. Thus, the linear extrapolation when $Bu \rightarrow 0$ is selected for the identified Nu/Nu_0 levels at $Bu = 0$ and $Ro>0$. But, due to the different channel configurations, the Nu/Nu_0 ratios measured from the rotating furrowed[32] and pin-fin[33] channels as depicted in **Figure 5** are respectively decreased and increased by raising *Bu*. In this regard, the depiction of Nu/Nu_0 variations against density ratio $(\Delta\rho/\rho)$[3,4,5,6,34] has often led to the non-linear Nu/Nu_0 variations. Thus, the extrapolation of each Nu/Nu_0 data trend at a fixed *Ro* toward the asymptotic limit of $\Delta\rho/\rho \rightarrow 0$ with diminished buoyancy effect along a non-linear data trend is often affected by the type of correlative function selected. Nevertheless, the data extrapolating procedure for the heat transfer results detected from the leading and trailing walls of the rotating channels[32] demonstrates the applicability to unravel the isolated Coriolis force effects on heat transfer properties with vanished buoyancy interaction at $Bu=0$ (**Figure 5**).

The so-called zero-buoyancy Nu/Nu_0 ratios are only controlled by *Ro* to reflect the isolated Coriolis force effects. The manner of heat transfer variations from the static-channel references disclosed by steps 7.7 and 7.8 is typified by **Figure 6**. The separated *Ro* impact from the buoyancy effect on the heat transfer performances of a rotating channel is correlated as the *Ro* function to be a part of Nu/Nu_0 correlation (**Figure 6**). The positive or negative ψ_2 values in **Figure 6** indicate the improving or impeding effects on heat transfer performances due to buoyancy interactions. The larger ψ_2 magnitude, the higher degrees of rotating buoyancy impact are imposed on the heat transfer properties. The fitted lines indicated in **Figure 6** are the plots of the correlative functions. The functional structures of the correlations for zero-buoyancy Nu/Nu_0 ratios and ψ_2 values are generally determined in accordance with the varying manners of the data trends emerged in **Figure 6**. As discussed previously, the different channel geometries between the furrowed[32] and pin-fin[33] channels have respectively led to the negative and positive ψ_2 values in **Figure 6**. But the common feature of the reduced magnitudes of ψ_2 values caused by increasing *Ro* is observed for the two types of rotating channels[32,33] in **Figure 6**. Having correlated the ψ_2 values and the Nu/Nu_0 ratios at zero-buoyancy conditions into the *Ro* functions, the heat transfer correlations, which permit the evaluation of the isolated and coupled *Ro* and *Bu* effects on Nu/Nu_0, is generated for the particular rotating channel.

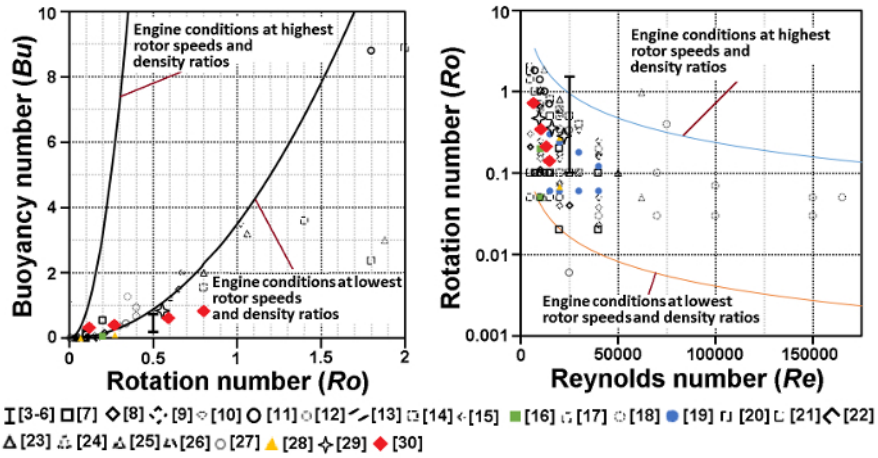

Figure 1. Realistic operating *Re*, *Ro* and *Bu* ranges and the emulated laboratory conditions for a rotating coolant channel in a gas turbine rotor blade. The test conditions performed by NASA HOST program[3,4,5,6] are indicated as the bar symbol. The open and solid symbols respectively signify the *Bu*, *Ro*, and *Re* test ranges for the pointed and full-field heat transfer measurements. Numbers in brackets are references from which data are taken. Please click here to view a larger version of this figure.

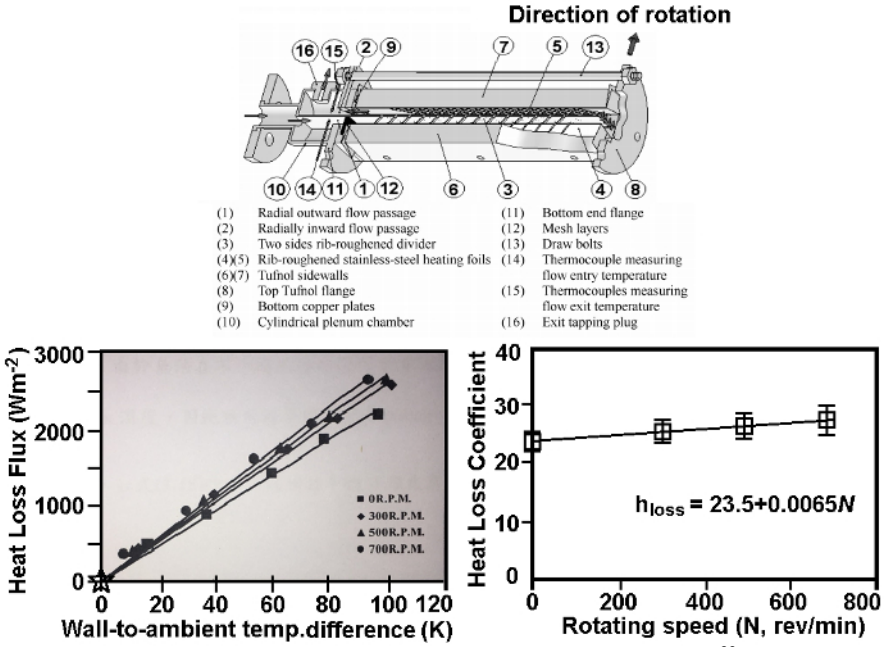

Figure 2. Typical heat loss coefficients (h_{loss}) at various rotating speeds[30] using the trapezoidal twin-pass rib-roughened rotating channel as an illustrative example. The diagram at the top depicts the constructional details of the rotating test module. The slope of each data trend constituted by the heat loss flux against the wall-to-ambient temperature difference shown in the left lower portion reveals the heat loss coefficient at the specific rotating speed. By correlating the heat loss coefficients detected at all the rotating speed tested, the generated heat loss correlation typified by the right lower plot is incorporated into the data processing program for *Nu* accountancy. The error bars in the lower right plot indicate the ranges of h_{loss}[30]. Please click here to view a larger version of this figure.

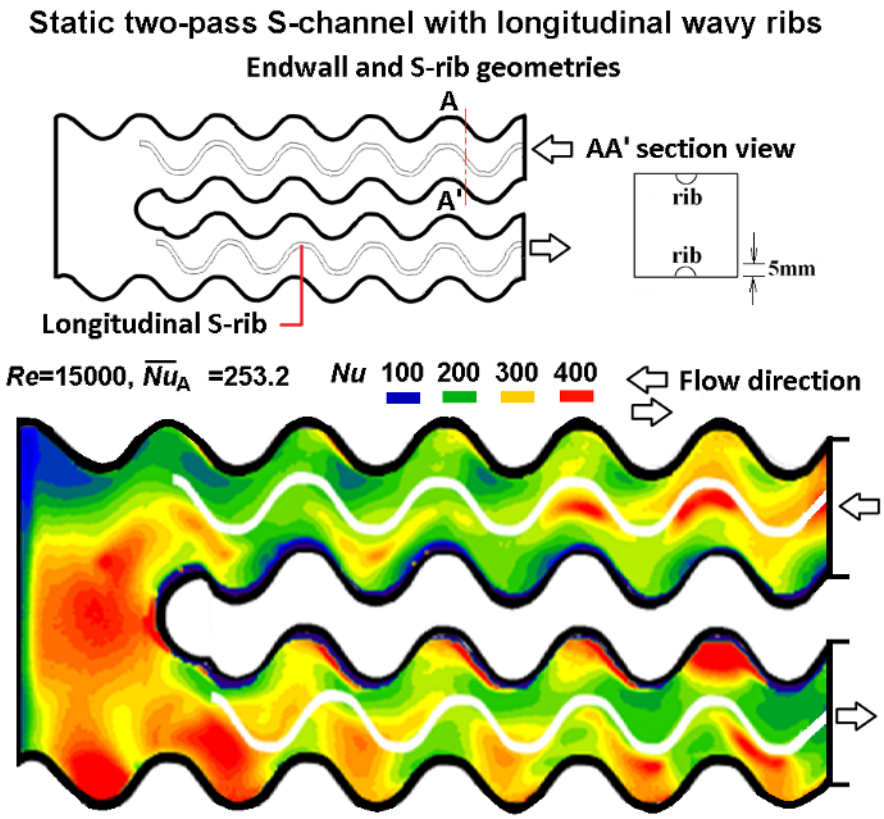

Figure 3. Local Nusselt number distribution of the static twin-pass S-channel roughened by curly ribs at *Re* = 15,000 measured by present infrared thermography method. The top diagram depicts the endwall of the two-pass wavy channel and the longitudinal S-ribs. As indicated by the AA' section view, the pair of longitudinal S-ribs is arranged inline on two opposite channel endwalls. In the detailed distribution of Nusselt number over the two-pass wavy endwall shown as the lower plot, the *Nu* data along the two longitudinal S-ribs are discarded due to the wall conduction effects on the distributions of heat-flux and wall-temperature. Please click here to view a larger version of this figure.

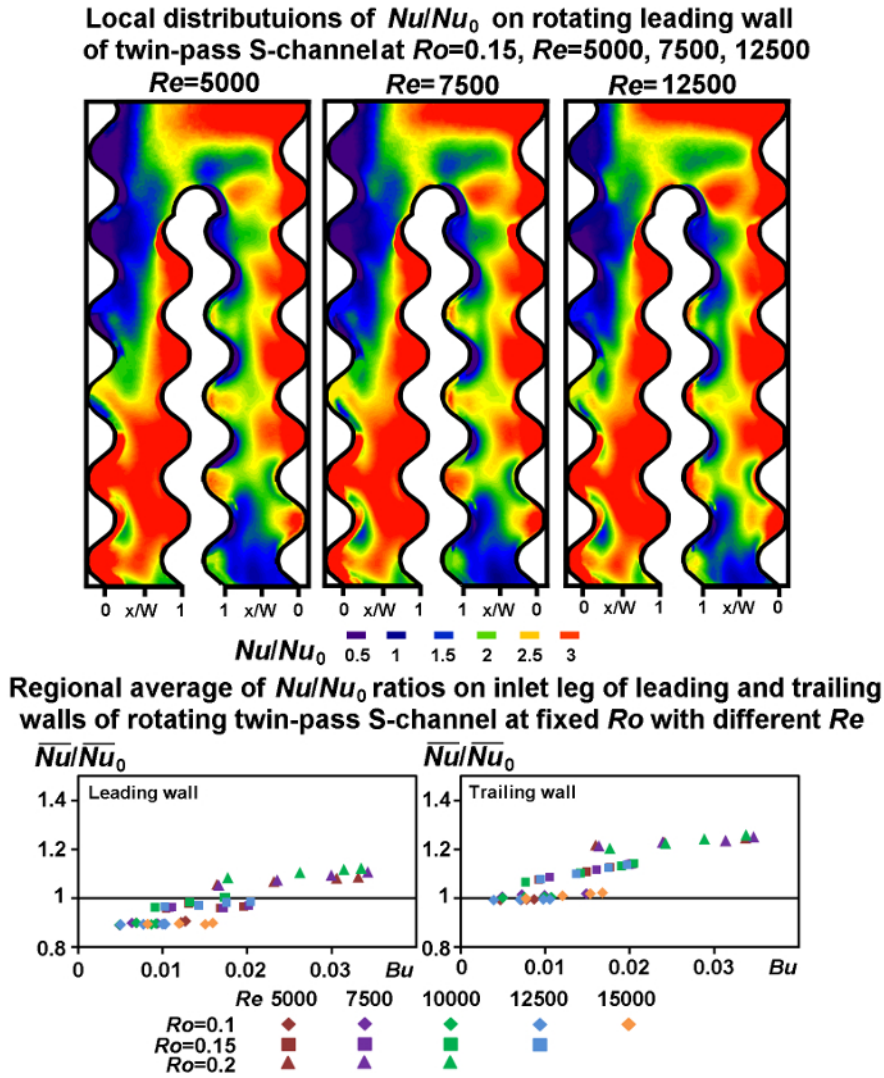

Figure 4. Examples demonstrating the isolation of *Re* impact from *Ro* and *Bu* effect on local and regionally-averaged heat transfer properties of rotating channel. The upper portion exhibits the detailed Nusselt number distributions at a fixed *Ro* of 0.15 with a different *Re* of 5000, 7500, and 12,500 to enlighten the impacts of Reynolds number on the heat transfer properties of the rotating endwall. The lower portion depicted the area-averaged heat transfer properties over the rotational leading and trailing endwalls. The normalized Nu/Nu_0 ratios highlight the heat transfer variations from the non-rotating scenarios by rotation. Adapted with permission from Chang *et al.* 2017[31]. Please click here to view a larger version of this figure.

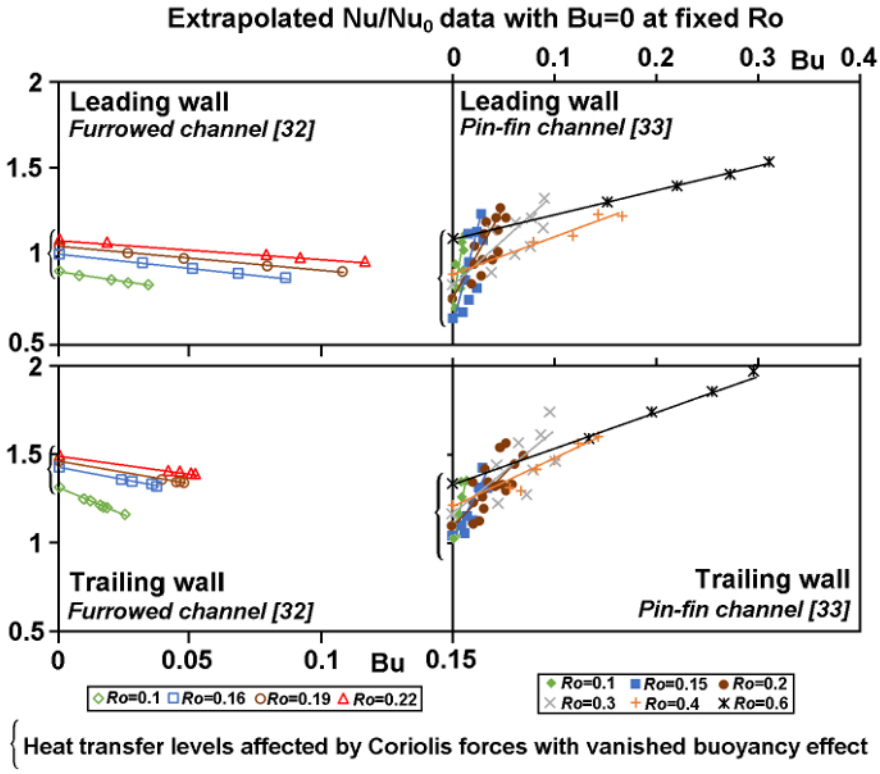

Figure 5. Examples demonstrating the uncoupled *Ro* effect from *Bu* impact on heat transfer properties of rotating channel[32,33]. Each *Bu*-driven Nu/Nu_0 variation is obtained at the fixed *Ro* and correlated as a linear function of *Bu* as indicated by the straight line in each plot. The correlation coefficients of these fitted lines fall between 0.96 and 0.98. The extrapolation of the Nu/Nu_0 data trend toward $Bu \rightarrow 0$ along each fitted line reveals the Nu/Nu_0 ratio at the tested *Ro*. The magnitude and slope of each *Bu*-driven Nu/Nu_0 data trend disclose the manners of buoyancy effect on heat transfer performances. The magnitudes of the slopes represent the degrees of *Bu* impact on Nu/Nu_0. The positive and negative slopes respectively reflect the improving and impairing buoyancy impact on heat transfer levels. Numbers in brackets are references from which data are taken. Please click here to view a larger version of this figure.

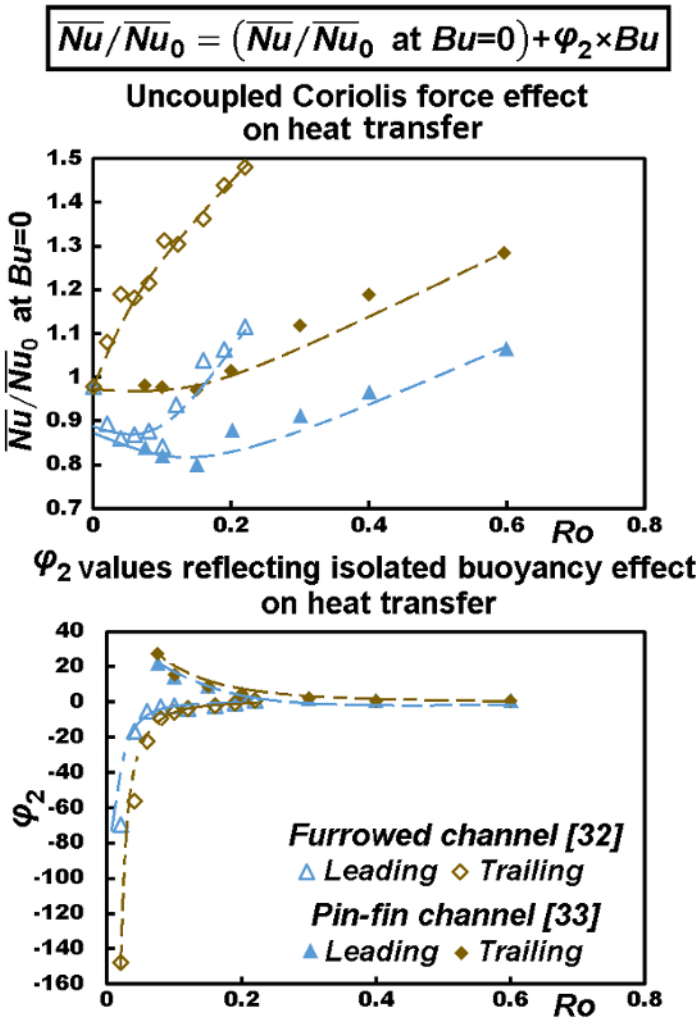

Figure 6. Uncoupled *Ro* and *Bu* effects on regionally averaged heat transfer performances of the rotating wavy channel[32,33]. The upper portion collects the heat transfer scenarios at various *Ro* but with vanished buoyancy effect at *Bu* = 0. Such Nu/Nu_0 variations are solely caused by the various Coriolis forces at different *Ro*. The lower portion shows the variations of *Bu* impact on Nu/Nu_0 at different *Ro*. The negative and positive ψ_2 values indicate the respective impairing and improving *Bu* impacts on the heat transfer performances for the furrowed[32] and pin-fin[33] channels. The dotted lines in this Figure are the correlation results for Nu/Nu_0 at *Bu* = 0. Numbers in brackets are references from which data are taken. Please click here to view a larger version of this figure.

Discussion

While the endwall temperatures of a rotating channel are detected by an infrared thermography system, the fluid temperatures are measured by thermocouples. As the alternative magnetic field of an AC motor that drives a rotating rig induces electrical potential to interfere the thermocouple measurements, the DC motor must be adopted to drive a rotating test rig.

The fluid temperature distribution over the exit plane of a heated channel is not uniform. At least five thermocouples on the existing plane of a rotating channel are recommended for measuring the local fluid exit temperatures. In particular, these thermocouples measuring the fluid temperatures installed in the flow passage are subject to centrifugal forces during the rotating tests. The thermocouple wires are easily bent toward the hot channel walls. Thus, a shielded thermocouple cable for measuring the fluid entry temperature is used. On the flow exit plane, a mesh with several thermocouple beads weaved on the mesh can be sandwiched between the exit flanges of a test channel to detect the fluid exit temperatures at the predefined locations under a rotating test condition.

With considerable rotation induced buoyancy effects on the flow and heat transfer characteristics of a rotating channel, the method selected to detect the full-field heat transfer data needs to include both Coriolis-force and buoyancy effects. Using the transient liquid crystal method for measuring the full-field heat transfer data, the thermal boundary layers are not yet fully developed as the temporal channel-wall temperature variations are essential by this method for acquiring the convective heat transfer coefficients. As the centripetal acceleration could reach 10^5 x g in a coolant channel of a rotating gas turbine blade, the heat transfer data subject to the influences of the fully developed buoyancy flows, which are detectable by the present experimental method, are more practical for design activities.

The exposure of the scanned hot channel wall to an infrared camera inevitably incurs heat loss from the Joule heat generated by the heating foils. The protocols for conducting the heat loss calibration tests are critical for ensuring the quality of heat transfer data. Inheriting either from the free or forced convective external flows for a static or rotating test channel, the convective heat transfer coefficients can be correlated as the function of wall-to-ambient temperature difference at a fixed rotating speed (**Figure 2**). It is preferable to envelop the entire rotating heat transfer test module with a shield for recovering the "free-convective" like external flows during the rotating tests. The maximum experimental uncertainties of heat transfer data are generally reduced when the percentage of the heat loss flux from the supplied heat flux is reduced. Nevertheless, the heat loss coefficients are slightly increased as *N* increases even with the enveloped shield covering the entire heat transfer test module (**Figure 3**). The heat loss correlation is included in the post data processing program to evaluate the distribution of local heat loss flux for each set of heat transfer test results. As the thermal inertia of the heat transfer module filled by thermal insulation material is considerably increased, the time required for reaching the steady-state condition during each heat loss test is considerably extended from a heat transfer test with airflow.

It is essential to investigate the applicability of the isolating *Re* effect on heat transfer properties from those induced by rotation. As the *Re* effect on heat transfer performances depends on the channel configurations, it is not appropriate to customarily adopt the heat transfer correlations generated from other channel geometries as the static-channel heat transfer references. The present experimental method isolates *Re* impact from *Ro* and *Bu* effects by presenting the heat transfer data in terms of Nu/Nu_0, in which the Nu_0 data are measured for the static test channel. While the buoyancy effect in a rotation channel with centripetal acceleration about 10^5 x g is considerable, the gravitation-driven buoyancy effect on the heat transfer property of a static channel is generally negligible within the typical range of fluid density ratios examined for a static test channel.

During a heat transfer test after feeding heater power to generate the required temperature gradients for facilitating heat convection, a certain degree of buoyancy effect driven by the induced centripetal acceleration field in the rotating channel is inevitable. Such coupled *Ro* and *Bu* effects for a rotating channel at the realistic engine conditions are not negligible due to the extremely high centripetal accelerations. Thus, both Coriolis force and rotating buoyancy level are simultaneously altered when the rotating speed is adjusted. The simultaneous control of *Ro* and *Re* at the targeting values during the rotating experiment is essential for decoupling the *Ro* and *Bu* effects on heat transfer properties. Having fixed both *Ro* and *Re*, the heat transfer variations corresponding to the variation of heat flux, or buoyancy level, reflect the rotating buoyancy effect on heat transfer properties at the tested *Ro*. The Nu/Nu_0 data converted from the data set generated in this manner permit the implementation of steps 7.4 - 7.8 for identifying the Coriolis force effect and rotating buoyance effect in isolation.

The *Bu* impact on the heat transfer property of a rotating channel is often *Ro* dependent as exemplified by **Figure 6** in which the ψ_2 values are varied as *Ro* changes. It is not appropriate to select the mathematic structure of the heat transfer correlation that treats the *Ro* and *Bu* as the independent parameters in the correlation.

In view of the Nu/Nu_0 extrapolation toward the limiting condition of $Bu \rightarrow 0$, the linear-like Nu/Nu_0 variations against the selected buoyancy parameter is preferable in order to reduce the uncertainty caused by the data extrapolation. In this regard, the fluid density ratio, $\Delta\rho/\rho$ or the buoyancy number, *Bu*, is recommended as the buoyancy parameter for disclosing the zero-buoyancy Nu/Nu_0 level during such data extrapolating process.

With high pressure rotating tests, the deformations of heating foils and the constituent components of a rotating channel due to the thermal expansions at various patterns of temperature distribution often cause airflow leakage during the rotating test. Such small airflow leakage is difficult to be identified during the rotating test. Thus, immediate subsequent data processing is recommended for acquiring the heat transfer data of the rotating channel. By cross-examining the heat transfer results obtained from the previous rotating tests, the implication of any inconsistent data trend is the possible airflow leakage. The subsequent measures to detect and then prevent the airflow leakage are required.

We have demonstrated a method for generating the heat transfer data of a rotating channel at the realistic engine conditions with the Coriolis-force effect and rotating buoyancy effect uncoupled. The major limitation of the present experimental method for extending the test ranges of *Ro* and *Bu* is the sustainability of the infrared camera that rotates with the test channel. In general, 10 x g is the maximum sustainable centrifugal acceleration for an infrared camera. With respect to the existing method detecting the heat transfer rates of a rotating channel, the use of thin heating foil can minimize the effects of channel-wall conduction on the distribution of local convective heat flux and the detection of temperatures at wall-fluid interfaces. Also, the two-dimensional full-field heat transfer distribution over a rotating surface subject to the steady-state buoyancy effect are detectable using the present experimental technique. With the data analysis method developed, the influences of Coriolis force and rotating buoyancy on the full-field heat transfer property of a rotating channel can be uncoupled. This method has already been applied to a wide range of rotating channel configurations. We expect that the present experimental strategy can lead to the design- friendly heat transfer correlations and which will continue to extend for the full coverage of realistic engine conditions when the advancement of infrared camera technology permits its usages at the conditions with higher centrifugal accelerations.

Disclosures

The authors have nothing to disclose.

Acknowledgements

The present research work was financially sponsored by the Ministry of Science and Technology of Taiwan under the grant NSC 94-2611-E-022-001, NSC 95-2221-E-022-018, NSC 96-2221-E-022-015MY3 and NSC 97-2221-E-022-013-MY3.

References

1. Morris, W.D. *Heat transfer and fluid flow in rotating coolant channels.* John Wiley and Sons, ISBN 0471101214 (1981).

2. Morris, W.D. A rotating facility to study heat transfer in the cooling passage of turbine rotor blades. *Journal of Power and Energy.* **210** (1), 55-63, (1996).
3. Wagner, J.H., Johnson, B.V., Graziani, R.A., Yeh, F.C. Heat transfer in rotating passages with smooth walls and radially outward flow. *ASME Journal of Turbomachinery.* **113** (1), 42-51, (1991).
4. Wagner, J.H., Johnson, B.V., Kopper, F.C. Heat transfer in rotating serpentine passages with smooth walls. *ASME Journal of Turbomachinery.* **113** (3), 321-330, (1991).
5. Wagner, J.H., Johnson, B.V., Steuber, G.D., Yeh, F.C. Heat transfer in rotating serpentine passages with trips normal to the flow. *ASME Journal of Turbomachinery.* **114** (4), 847-857, (1992).
6. Johnson, B.V., Wagner, J.H., Steuber, G.D., Yeh, F.C. Heat transfer in rotating serpentine passages with selected model orientations for smooth or skewed trip walls. *ASME Journal of Turbomachinery.* **116** (4), 738-744, (1992).
7. Hwang, G.J., Tzeng, S.C., Mao, C.P., Soong, C. Y. Heat transfer in a radially rotating four-pass serpentine channel with staggered half-v rib turbulators. *ASME Journal of Heat Transfer.* **123** (1), 39-50, (2001).
8. Azad, G.S., Uddin, M.J., Han, J.C., Moon, H.K., Glezer, B. Heat transfer in a two-pass rectangular rotating channel with 45-deg angled rib turbulators. *ASME Journal of Turbomachinery.* **124** (2), 251-259, (2002).
9. Griffith, T.S., Al-Hadhrami, L., Han, J.C. Heat transfer in rotating rectangular cooling channels (AR=4) with angled ribs. *ASME Journal of Heat Transfer.* **124** (4), 617-625, (2002).
10. Al-Hadhrami, L., Griffith, T.S., Han, J.C. Heat transfer in two-pass rotating rectangular channels (AR=2) with five different orientations of 45 deg V-shaped rib turbulators. *ASME Journal of Heat Transfer.* **125** (2), 232-242, (2003).
11. Chang, S.W., Liou, T.M., Hung, J.H., Yeh, W.H. Heat transfer in a radially rotating square-sectioned duct with two opposite walls roughened by 45 deg staggered ribs at high rotation numbers. *ASME Journal of Heat Transfer.* **129** (2), 188-199, (2007).
12. Zhou, F., Lagrone, J., Acharya, S. Internal cooling in 4:1 AR passages at high rotation numbers. *ASME Journal of Heat Transfer.* **129** (12), 1666-1675, (2007).
13. Liu, Y.H., Huh, M., Han, J.C., Chopra, S. Heat transfer in a two-pass rectangular channel (AR=1:4) under high rotation numbers. *ASME Journal of Heat Transfer.* **130** (8), 081701-1-9, (2008).
14. Chang, S.W., Liou, T.M., Chiou, S.F., Chang, S.F. Heat transfer in high-speed rotating trapezoidal duct with rib-roughened surfaces and air bleeds from the wall on the apical side. *ASME Journal of Heat Transfer.* **130** (6), 061702-1-13, (2008).
15. Wright, L.M., Liu, Y.H., Han, J.C., Chopra, S. Heat transfer in trailing edge, wedge-shaped cooling channels under high rotation numbers. *ASME Journal of Heat Transfer.* **130** (7), 071701-1-11, (2008).
16. Liou, T.M., Chen, M.Y., Tsai, M.H. Fluid flow and heat transfer in a rotating two-pass square duct with in-line 90-deg ribs. *ASME Journal of Turbomachinery.* **124** (2), 260-268, (2002).
17. Chang, S.W., Liou, T.M., Yang, T.L., Hong, G.F. Heat transfer in radially rotating pin-fin channel at high rotation numbers. *ASME Journal of Turbomachinery.* **132** (2), 021019-1-12, (2010).
18. Rallabandi, A., Lei, J., Han, J.C., Azad, S., Lee, C.P. Heat transfer measurements in rotating blade-shape serpentine coolant passage with ribbed walls at high Reynolds numbers. *ASME Journal of Turbomachinery.* **136** (9), 091004-1-9, (2014).
19. Mayo, I., Arts, T., Ahmed, E.H., Parres, B. Two-dimensional heat transfer distribution of a rotating ribbed channel at different Reynolds numbers. *ASME Journal of Turbomachinery.* **137** (3), 031002-1-11, (2015).
20. Chang, S.W., Yang, T.L., Liou, T.M., Fang, H.G. Heat transfer in rotating scale-roughened trapezoidal duct at high rotation numbers. *Applied Thermal Engineering.* **29** (8), 1682-1693, (2009).
21. Liou, T. M., Chang, S.W., Chen, J.S., Yang, T.L., Lan, Y.A. Influence of channel aspect ratio on heat transfer in rotating rectangular ducts with skewed ribs at high rotation numbers. *International Journal of Heat Mass Transfer.* **52** (23), 5309-5322, (2009).
22. Huh, M., Liu, Y.H., Han, J.C. Effect of rib height on heat transfer in a two pass rectangular channel (AR = 1:4) with a sharp entrance at high rotation numbers. *International Journal of Heat Mass Transfer.* **52** (19), 4635-4649, (2009).
23. Xu, G., Li, Y., Deng, H. Effect of rib spacing on heat transfer and friction in a rotating two-pass square channel with asymmetrical 90-deg rib turbulators. *Applied Thermal Engineering.* **80** (5), 386-395, (2015).
24. Tao, Z., Yang, M., Deng, H., Li, H., Tian, S. Heat transfer study in a rotating ribbed two-pass channel with engine-similar cross section at high rotation number. *Applied Thermal Engineering.* **106** (5), 681-696, (2016).
25. Li, Y., Deng, H., Tao, Z., Xu, G., Chen, Y. Heat transfer characteristics in a rotating trailing edge internal cooling channel with two coolant inlets. *International Journal of Heat Mass Transfer.* **105** (2), 220-229, (2017).
26. Deng, H., Chen, Y., Tao, Z., Li, Y., Qiu, L. Heat transfer in a two-inlet rotating rectangular channel with side-wall fluid extraction. *International Journal of Heat and Mass Transfer.* **105** (2), 525-534, (2017).
27. You, R., Li, H., Tao, Z., Wei, K. Heat transfer investigation in a smooth rotating channel with thermography liquid crystal. ASME Turbo Expo. GT2016-56413. *Turbomachinery Technical Conference and Exposition: Heat Transfer.* **5** (B), V05BT16A006 1~10, (2016).
28. Morris, W.D., Chang, S.W. An experimental study of heat transfer in a simulated turbine blade cooling passage. *International Journal of Heat Mass Transfer.* **40** (15), 3703-3716, (1997).
29. Chang, S.W., Liou, T.-M., Po., Y. Coriolis and rotating buoyancy effect on detailed heat transfer distributions in a two-pass square channel roughened by 45° ribs at high rotation numbers. *International Journal of Heat Mass Transfer.* **53** (7), 1349-1363, (2010).
30. Wang, W.J. *Heat transfer in rotating twin-pass trapezoidal-sectioned passage with two opposite walls roughened by 45 degree ribs.* Msc thesis, Department of Marine Engineering, National Kaohsiung Marine University, (2006).
31. Chang, S.W., Wu, P.-S., Chen, C.-S., Weng, C.-C., Jiang, Y.-R., Shih, S.-H. Thermal performance of radially rotating two-pass S-shaped zig-zag channel. *International Journal of Heat and Mass Transfer.* **115** (B), 1011-1031, (2017).
32. Chang, S.W., Lees, A. W., Liou, T.-M., Hong, G.F. Heat transfer of a radially rotating furrowed channel with two opposite skewed sinusoidal wavy walls. *International Journal of Thermal Sciences.* **49** (5), 769-785, (2010).
33. Chang, S.W., Liou, T.-M., Lee, T.-H, Heat transfer of a rotating rectangular channel with a diamond-shaped pin-fin array at high rotation numbers. *Journal of Turbomachinery Transactions of the ASME.* **135** (4), 041007 1~10, (2013).
34. Morris, W.D., Chang, S.W., Heat transfer in a radially rotating smooth-walled tube. *The Aeronautical Journal.* **102** (1015), 277-285, (1998).

